A Stochastic Skeleton Model for the MJO

Sulian Thual [(1)], Andrew J. Majda [(1)], and Samuel N. Stechmann [(2)]

(1) Department of Mathematics, and Center for Atmosphere Ocean Science, Courant Institute of Mathematical Sciences, New York University, 251 Mercer Street, New York, NY 10012 USA

(2) Department of Mathematics, and Department of Atmospheric and Oceanic Sciences, University of Wisconsin - Madison, 480 Lincoln Drive, Madison, WI 53706 USA

Corresponding author:

Sulian Thual, 251 Mercer Street, New York, NY 10012 USA, *sulian.thual@gmail.com*

Abstract

The Madden-Julian oscillation (MJO) is the dominant mode of variability in the tropical atmosphere on intraseasonal timescales and planetary spatial scales. Despite the primary importance of the MJO and the decades of research progress since it original discovery, a generally accepted theory for its essential mechanisms has remained elusive. In recent work by two of the authors, a minimal dynamical model has been proposed that recovers robustly the most fundamental MJO features of (I) a slow eastward speed of roughly $5\,ms^{-1}$, (II) a peculiar dispersion relation with $d\omega/dk \approx 0$, and (III) a horizontal quadrupole vortex structure. This model, the skeleton model, depicts the MJO as a neutrally-stable atmospheric wave that involves a simple multiscale interaction between planetary dry dynamics, planetary lower-tropospheric moisture, and the planetary envelope of synoptic-scale activity. In this article, we show that the skeleton model can further account for (IV) the intermittent generation of MJO events and (V) the organization of MJO events into wave trains with growth and

demise, as seen in nature. We achieve this goal by developing a simple stochastic parametrization for the unresolved details of synoptic-scale activity, that is coupled to otherwise deterministic processes in the skeleton model. In particular, the intermittent initiation, propagation and shut down of MJO wave trains in the skeleton model occur through these stochastic effects. This includes examples with a background warm-pool where some initial MJO-like disturbances propagate through the western region but stall at the peak of background convection/heating corresponding to the maritime continent in nature.

1 Introduction

The dominant component of intraseasonal variability in the tropics is the 40 to 50 day tropical intraseasonal oscillation, often called the Madden-Julian oscillation (MJO) after its discoverers (Madden and Julian, 1971; Madden and Julian, 1994). In the troposphere, the MJO is an equatorial planetary-scale wave, that begins as a standing wave in the Indian Ocean and propagates eastward across the western Pacific ocean at a speed of around $5\,ms^{-1}$. The planetary-scale circulation anomalies associated with the MJO significantly affect monsoon development, intraseasonal predictability in midlatitudes, and the development of the El Niño events in the Pacific ocean, which is one of the most important components of seasonal prediction.

Despite the primary importance of the MJO and the decades of research progress since its original discovery, no theory for the MJO has yet been generally accepted, and the problem of explaining the MJO has been called the search for the Holy Grail of tropical atmospheric dynamics (Raymond, 2001). Simple theories provide some useful insight on certain isolated aspects of the MJO, but they have been largely unsuccessful in reproducing all of its fundamental features together (Zhang, 2005). Meanwhile, present-day simulations by general circulation models (GCMs) typically have poor representations of it (Lin et al., 2006; Kim et al., 2009). A growing body of evidence suggests that this poor performance of both theories and simulations in general is due to the inadequate treatment of the organized hierarchy of tropical processes as a whole (e.g. Hendon and Liebmann, 1994; Zhang, 2005; Moncrieff et al., 2007; Lau and Waliser,

2012). This hierarchy involves interactions between organized structures of tropical convection (convectively-coupled waves, cloud-clusters...), that are defined on a vast range of spatiotemporal scales (synoptic, mesoscale...) and that generate the MJO as their planetary envelope .

This organized hierarchy of tropical processes is the focus of various observational initiatives and modeling studies. The challenges to deal with are two-fold. First, there is a general lack of theoretical understanding of this hierarchy and of its relation to the MJO. For instance, insight has been gained from the study of MJO-like waves in multicloud model simulations and in superparametrization computer simulations, which appear to capture many of the observed features of the MJO by accounting for smaller-scale convective structures within the MJO envelope (Grabowski, 2001; Grabowski and Moncrieff, 2004; Moncrieff, 2004; Majda et al., 2007; Khouider and Majda, 2007). In fact, the multicloud model coupled to a state of the art GCM with coarse resolution has been shown to produce a MJO with realistic structure in idealized simulations (Khouider et al., 2011). As another example, the role of synoptic scale waves in producing key features of the MJO's planetary scale envelope has been elucidated in multiscale asymptotic models (Majda and Biello, 2004; Biello and Majda, 2005; Majda and Stechmann, 2009a; Stechmann et al., 2013). Secondly, a consequent limitation of current GCMs and models in general that simulate the MJO is the resolution of small scale moist processes. In these models computing resources significantly limit spatial resolution (to $\approx 10 - 100\,km$), and there are therefore several important small scales that are unresolved or parametrized according to various recipes. As regards tropical convection, unresolved processes at smaller scales such as deep convective clouds show some particular features in space and time, such as high irregularity, high intermittency and low predictability. Some good candidates to account for those processes while remaining computationally efficient appear to be suitable stochastic parametrizations (Majda et al., 2008; Palmer, 2012). Generally speaking, these models consist in coupling some simple stochastic triggers (e.g., birth/death, spin-flip, coarse-grained lattice models...) to the otherwise deterministic processes, according to some probability laws motivated by physical intuition gained (elsewhere) from observations and detailed numerical simulations (Gardiner, 1994; Katsoulakis et al., 2003; Lawler, 2006). This methodology has been successful in parametrizing with more realism some essential processes of tropical vari-

ability, in a broad range of applications (Majda and Khouider, 2002; Khouider et al., 2003; Majda and Stechmann, 2008; Khouider et al., 2010; Stechmann and Neelin, 2011; Frenkel et al., 2012; Frenkel et al., 2013). A particular focus of the present article is the relevance of such methodology to the MJO.

While theory and simulation of the MJO remain difficult challenges, they are guided by some generally accepted, fundamental features of the MJO on intraseasonal-planetary scales that have been identified relatively clearly in observations (Hendon and Salby, 1994; Wheeler and Kiladis, 1999; Zhang, 2005). These features are referred to here as the MJO's "skeleton" features (Majda and Stechmann, 2009b):

I. A slow eastward phase speed of roughly $5\,ms^{-1}$,

II. A peculiar dispersion relation with $d\omega/dk \approx 0$, and

III. A horizontal quadrupole structure.

Recently, Majda and Stechmann (2009b) introduced a minimal dynamical model, the skeleton model, that captures the MJO's intraseasonal features (I-III) together for the first time in a simple model. The model is a nonlinear oscillator model for the MJO skeleton features and the skeleton features of tropical intraseasonal variability in general. It depicts the MJO as a neutrally-stable atmospheric wave that involves a simple multiscale interaction between (i) planetary-scale, dry dynamics, (ii) planetary-scale, lower-tropospheric moisture and (iii) the planetary envelope of synoptic-scale convection/wave activity. In particular, there is no instability mechanism at planetary scale, and the interaction with sub-planetary processes (iii) discussed above is accounted for, at least in a crude fashion (see alternatively Wang and Liu, 2011; Liu and Wang, 2012).

While the features (I-III) are the salient intraseasonal-planetary features of MJO composites, individual MJO events often have unique features beyond the MJO's skeleton. These features are referred to here as the MJO's "muscle" features (Majda and Stechmann, 2009b). They include for example refined zonal and vertical structures as well as complex dynamic and convective features within the MJO envelope (e.g., front-to-rear vertical tilts, westerly wind bursts...), with characteristics and intensity that differ from one MJO event to another (Kikuchi and Takayabu, 2004;

Kiladis et al., 2005; Tian et al., 2006; Kiladis et al., 2009). Majda and Stechmann (2011) has shown that the skeleton model, despite its minimal design, can account qualitatively for certain of these MJO's "muscle" features in suitable settings. In an collection of numerical experiments, the non-linear skeleton model has been shown to simulate MJO events with significant variations in occurrence and strength, asymmetric east-west structures, as well as a preferred localization over the background state warm pool region.

In the present article, the goal is to account qualitatively for more realistic MJO's "muscle" features within the skeleton model. Two particular features of interest that we will recover are

IV. The intermittent generation of MJO events, and

V. The organization of MJO events into wave trains with growth and demise.

These features, though essential to our understanding of the MJO, remain quite elusive. There is for example an on-going discussion on assessing to which extent the MJO events are either generated as resulting from the internal variability of certain tropical processes or as a secondary response to independently existing extratropical forcings (Zhang, 2005; Lau and Waliser, 2012). A related question is why this generation is highly intermittent, with sometimes some clearly identified precursors and sometimes few or none (Matthews, 2008; Straub, 2013). In addition, the MJO events as observed in nature tend to organize into wave trains i.e. into series of successive MJO events, either two, three, or sometimes more in a row (Matthews, 2008; Yoneyama et al., 2013). There is notably a general lack of understanding of the processes controlling the growth and demise of those wave trains.

Here, we will show that features (IV) and (V) can be accounted for only from the internal variability of a few essential tropical processes such as the ones depicted in the skeleton model. To achieve this goal, we will embed within the skeleton model a simple yet suitable stochastic parametrization, namely a birth/death process (the simplest continuous-time Markov process), that will allow for an intermittent evolution of (iii) the planetary envelope of synoptic activity (Gardiner, 1994; Lawler, 2006). This stochastic parametrization follows the same prototype found in the related studies mentioned above (e.g. as reviewed in Majda et al., 2008). However, while those studies usually focus on parametrizing unresolved mesoscale processes (the ones unresolved

in GCMs), the stochastic parametrization proposed here is intended at the unresolved synoptic processes in the skeleton model. Synoptic scale processes are a complex menagerie of convectively coupled equatorial waves, such as 2-day waves, convectively coupled Kelvin waves, etc, with high irregularity and intermittency (Kiladis et al., 2009). Some of these synoptic details (but not all) are important to the MJO, as they can be both modulated by the planetary background state and contribute to it, for example through upscale convective momentum transport or enhanced surface heat fluxes (Majda and Biello, 2004; Biello and Majda, 2005; Majda and Stechmann, 2009a; Stechmann et al., 2013; Dias et al., 2013).

In the present article, we will document to what extent this "stochastic skeleton model" with minimal design and stochastic parametrization accounts for both the features (I-III) and (IV-V) in suitable simulation settings. We will consider two simulations in statistically equilibrated regime, one with a homogeneous background state and one with a background state representative of the equatorial warm pool.

The article is organized as follows. In section 2 we recall the design and main features of the skeleton model, and present the stochastic version used here. In section 3 we present the solutions of the stochastic skeleton model for a homogeneous background state. In section 4 we present the solutions in different settings with a background state representative of the equatorial warm pool. Section 5 is a discussion with concluding remarks. In appendix A we detail the numerical method, and in appendix B we briefly summarize some additional sensitivity tests that show the robustness of results to changes in model parameters.

2 Summary of the Skeleton Model

2.1 Non-linear Skeleton Model

The skeleton model has been originally proposed by Majda and Stechmann (2009b) (hereafter MS009), and further analyzed in Majda and Stechmann (2011) (hereafter MS2011). It is a minimal non-linear oscillator model, defined at planetary scale, that depicts the MJO as a neutrally stable wave. The fundamental assumption in the skeleton model is that the MJO involves a sim-

ple multiscale interaction between (i) planetary-scale, dry dynamics, (ii) planetary-scale, lower-tropospheric moisture and (iii) synoptic-scale, convection/wave activity. The last quantities (ii) and (iii) in particular are represented by the variables q and a, respectively:

- q: Lower-tropospheric moisture anomalies.

- a: Amplitude of the envelope of synoptic activity.

Note that both quantities are defined at planetary-scale: the planetary envelope a in particular is a collective (i.e. integrated) representation of the convection/wave activity occurring at synoptic-scale, the details of which are unresolved. A key part of the $q - a$ interaction is how moisture anomalies influence convection. Rather than a functional relationship $a = a(q)$, it is assumed that q influences the tendency (i.e. the growth and decay rates) of the envelope of synoptic activity. The simplest design that embodies this idea is the following (non-linear) amplitude equation:

$$\partial_t a = \Gamma q a \,, \tag{1}$$

where $\Gamma > 0$ is a constant of proportionality: positive (negative) low-level moisture anomalies create a tendency to enhance (decrease) the envelope of synoptic activity.

The basis for equation (1) comes from a combination of observations, modeling, and theory. Generally speaking, it is well-known that tropospheric moisture content plays a key role in regulating convection (Grabowski and Moncrieff, 2004; Moncrieff, 2004; Holloway and Neelin, 2009). In observations, specifically on intraseasonal-planetary scales, several studies have shown that the lower troposphere tends to moisten during the suppressed convection phase of the MJO and that lower-tropospheric moisture leads the MJO's heating anomaly, which suggests the relationship in equation (1) (Kikuchi and Takayabu, 2004; Kiladis et al., 2005; Tian et al., 2006). This relationship is further suggested by simplified models for synoptic-scale convectively coupled waves showing that the growth rates of the convectively coupled waves depend on the wave's environment, such as the environmental moisture content (Khouider and Majda, 2006; Majda and Stechmann, 2009a; Stechmann et al., 2013). Stechmann et al. (2013) in particular estimates the value of Γ from these growth rate variations.

In the skeleton model, the $q-a$ interaction parametrized in equation (1) is further combined with the linear primitive equations. This reads, in non-dimensional units,

$$
\begin{aligned}
&\partial_t u - yv = -\partial_x p \\
&yu = -\partial_y p \\
&0 = -\partial_z p + \theta \\
&\partial_x u + \partial_y v + \partial_z w = 0 \\
&\partial_t \theta + w = \overline{H} a - s^\theta \\
&\partial_t q - \overline{Q} w = -\overline{H} a + s^q \\
&\partial_t a = \Gamma q a \,,
\end{aligned}
\tag{2}
$$

with periodic boundary conditions along the equatorial belt. The five first rows of equation (2) describe the dry atmosphere dynamics, with equatorial long-wave scaling as allowed at planetary scale. The u, v, and w are the zonal, meridional, and vertical velocity, respectively; and p and θ are the pressure and potential temperature, respectively. The sixth row describes the evolution of low-level moisture q, and the seventh row is the non-linear amplitude equation for a described previously. All variables are anomalies from a radiative-convective equilibrium, except a. The interactions between those various components is through the envelope of synoptic activity, a, which is assumed to act at planetary-scale as a balanced source of both heating and drying. This model contains a minimal number of parameters: $\overline{Q}$ is the background vertical moisture gradient, Γ is a proportionality constant. The $\overline{H}$ is irrelevant to the dynamics (as can be seen by rescaling a) but permits to define a heating/drying rate $\overline{H}a$ for the system in dimensional units. The s^θ and s^q are external sources of cooling and moistening, respectively, that need to be prescribed in the system (see hereafter).

To obtain the skeleton model in its simplest form, it is necessary to truncate the system from equation (1) to the first vertical and meridional structures. For this flow trapped within the equatorial troposphere the relevant structures are the first vertical baroclinic mode and the first meridional Hermite function (Majda, 2003). First, we project and truncate at the first baroclinic mode, such that $u(x,y,z,t) = u(x,y,t)\sqrt{2}cos(z)$, $\theta(x,y,z,t) = \theta(x,y,t)\sqrt{2}sin(z)$, etc., with a

slight abuse of notation. The skeleton model now reads:

$$
\begin{aligned}
&\partial_t u - yv - \partial_x \theta = 0 \\
&yu - \partial_y \theta = 0 \\
&\partial_t \theta - (\partial_x u + \partial_y v) = \overline{H} a - s^\theta \\
&\partial_t q + \overline{Q}(\partial_x u + \partial_y v) = -\overline{H} a + s^q \\
&\partial_t a = \Gamma q a \,,
\end{aligned}
\tag{3}
$$

where the dry dynamics component is now a time-dependent and non-dissipative version of the Matsuno-Gill model (Matsuno, 1966; Gill, 1980). Second, we project and truncate at the first Hermite function, such that $a(x,y,t) = A(x,t)\phi_0$, $q = Q\phi_0$, $s^q = S^q\phi_0$, $s^\theta = S^\theta\phi_0$, where $\phi_0(y) = \sqrt{2}(4\pi)^{-1/4} exp(-y^2/2)$. A suitable change of variables for the dry dynamics component is to introduce K and R, which are the amplitudes of the equatorial Kelvin wave and of the equatorial Rossby first symmetric wave, respectively. Indeed, those equatorial waves are the only ones excited by the meridional heating structures on ϕ_0, and are easily solved. The skeleton model now reads

$$
\begin{aligned}
&\partial_t K + \partial_x K = (S^\theta - \overline{H} A)/2 \\
&\partial_t R - \partial_x R/3 = (S^\theta - \overline{H} A)/3 \\
&\partial_t Q + \overline{Q}(\partial_x K - \partial_x R/3) = (\overline{H} A - S^q)(\overline{Q}/6 - 1) \\
&\partial_t A = (\Gamma\gamma) Q A \,,
\end{aligned}
\tag{4}
$$

with variables K, R, Q, and A. The $\gamma \approx 0.6$ is a cross-term resulting from the meridional projection of the non-linear amplitude equation. The variables of the dry dynamics component can be reconstructed a-posteriori using

$$
\begin{aligned}
u &= [K - R]\phi_o + R\phi_2/\sqrt{2} \\
v &= [4\partial_x R - \overline{H} A]\phi_1/3\sqrt{2} \\
\theta &= -[K + R]\phi_o - R\phi_2/\sqrt{2} \,,
\end{aligned}
\tag{5}
$$

where the next Hermite functions read $\phi_1(y) = 2y(4\pi)^{-1/4}exp(-y^2/2)$, and $\phi_2(y) = (2y^2 - 1)(4\pi)^{-1/4}exp(-y^2/2)$. The components ϕ_1 and ϕ_2 are irrelevant to the dynamics, yet they are necessary to retrieve the quadrupole structure of the MJO (see figure 3 of MS2009). Note that they are slight differences in notation with respect to MS2009 and MS2011, where A stands for anomalies, the cross-term γ is absorbed into Γ, and the amplitudes K and R are chosen differently (as $\sqrt{2}K$ and $2\sqrt{2}R$ in comparison).

We recall briefly the main properties of the skeleton model for the MJO, and the reader is invited to refer to MS2009 and MS2011 for further details. The skeleton model is designed following two important principles of energy conservation. For balanced external sources of cooling/moistening $s^\theta = s^q$, the system in equation (3) conserves a vertically integrated moist static energy

$$\partial_t(\theta + q) - (1 - \overline{Q})(\partial_x u + \partial_y v) = 0\,, \tag{6}$$

and further conserves a total positive energy (as there are no dissipative processes)

$$\partial_t \left[\frac{1}{2}u^2 + \frac{1}{2}\theta^2 + \frac{1}{2}\frac{\overline{Q}}{1-\overline{Q}}\left(\theta + \frac{q}{\overline{Q}}\right)^2 + \frac{\overline{H}}{\Gamma\overline{Q}}a - \frac{s^\theta}{\Gamma\overline{Q}}\log(a) \right] - \partial_x(u\theta) - \partial_y(v\theta) = 0\,. \tag{7}$$

The linear waves of the skeleton model are shown in figure 1, as computed from the reference parameter values used in this article (see hereafter). They are four eigenmodes that are, in order of decreasing phase speed: the dry Kelvin mode ($\approx 55\,ms^{-1}$), the MJO mode ($\approx 5\,ms^{-1}$), the moist Rossby mode ($\approx -3\,ms^{-1}$) and the dry Rossby mode ($\approx -20\,ms^{-1}$). All four of the linear modes are neutrally stable. The MJO mode in particular captures the fundamental features of the observed MJO such as a slow eastward phase speed and an oscillation frequency that is roughly constant. As seen on the associated eigenmode amplitudes, the MJO mode consists of coupled interactions between the equatorial waves K, R (dominant at small wavenumber) and the moisture and synoptic activity components Q, A (dominant at large wavenumber). At small wavenumber in particular the physical structure of the MJO mode is a horizontal quadrupole vortex structure, as seen in nature (not shown, see figure 3 of MS2009).

2.2 Stochastic Skeleton Model

We now introduce the stochastic skeleton model that is a modified version of the skeleton model with a simple stochastic parametrization of the synoptic scale processes. In the skeleton model, the MJO results from a simple multiscale interaction between (i) the planetary-scale dynamics and (ii) moisture and (iii) the planetary envelope of synoptic activity (see discussion above). The details of synoptic activity are, however, unresolved. They consist of a complex menagerie of convectively coupled equatorial waves, such as 2-day waves, convectively coupled Kelvin waves, etc (Kiladis et al., 2009). Some of these synoptic details (but not all) are important to the MJO, as they can be both modulated by the planetary background state and contribute to it, for example through upscale convective momentum transport or enhanced surface heat fluxes (Majda and Biello, 2004; Biello and Majda, 2005; Majda and Stechmann, 2009a; Stechmann et al., 2013). With respect to the planetary processes depicted in the skeleton model, the contribution of those synoptic details appears most particularly to be highly irregular, intermittent, and with a low predictability. To account for this intermittent contribution while keeping the minimal design of the skeleton model (i.e., without solving entirely the synoptic details), one suitable strategy is to develop a stochastic parametrization of the synoptic scale processes.

For such a stochastic parametrization, a simple yet non trivial design is to implement a stochastic birth/death process (the simplest continuous-time Markov process) controlling the evolution of the envelope of synoptic activity a (see chapter 7 of Gardiner, 1994; Lawler, 2006). Let a be a random variable taking discrete values $a = \Delta a\, \eta$, where η is a non-negative integer. The birth/death process allows for intermittent transitions between the states η, accounting here for intermittent changes in the envelope of synoptic activity. The probabilities of transiting from one state η to another over a time step Δt read as follows:

$$
\begin{aligned}
&P\{\eta(t+\Delta t) = \eta(t) + 1\} = \lambda \Delta t + o(\Delta t) \\
&P\{\eta(t+\Delta t) = \eta(t) - 1\} = \mu \Delta t + o(\Delta t) \\
&P\{\eta(t+\Delta t) = \eta(t)\} = 1 - (\lambda + \mu)\Delta t + o(\Delta t) \\
&P\{\eta(t+\Delta t) \neq \eta(t) - 1,\, \eta(t),\, \eta(t) + 1\} = o(\Delta t)\,,
\end{aligned}
\tag{8}
$$

where λ and μ are the upward and downward rates of transition, respectively. The envelope of synoptic activity can intermittently increase at rate λ or decrease at rate μ. This can alternatively be expressed in the form of a master equation

$$\partial_t P(\eta) = [\lambda(\eta-1)P(\eta-1) - \lambda(\eta)P(\eta)] + [\mu(\eta+1)P(\eta+1) - \mu(\eta)P(\eta)]\,, \tag{9}$$

where $P(\eta)$ is the probability of the state η (not to be mistaken with the conditional probabilities in equation (8)). There are various possible ways to choose the transition rates μ and λ. Here, the design principle is that the dynamics of the skeleton model presented previously must be recovered on average. In the asymptotic limit of small transitions Δa, the mean-field equation associated to equation (9) must read:

$$\partial_t E(a) = \Gamma E(qa)\,, \tag{10}$$

where E denotes the statistical expected value. One simple and practical choice of the transition rates that satisfies this design principle is as follows:

$$\lambda = \begin{cases} \Gamma|q|\eta + \delta_{\eta 0} \text{ if } q \geq 0 \\ \delta_{\eta 0} \text{ if } q < 0 \end{cases} \quad \text{and } \mu = \begin{cases} 0 \text{ if } q \geq 0 \\ \Gamma|q|\eta \text{ if } q < 0 \end{cases} \tag{11}$$

Note that the upward and downward rates λ and μ depend here on the system variables η and q, which is characteristic of a multiplicative noise. The kronecker delta operator $\delta_{\eta 0}$ ensures that $\lambda = 1$ when $\eta = 0$ such that there is no finite-time extinction, and is null otherwise. The associated mean-field equation reads

$$\partial_t E(a) = \Delta a\, E(\lambda + \mu) = \Gamma E(qa) + \Delta a\, E(\delta_{\eta 0}) \tag{12}$$

which is identical to the desired mean-field equation (10) in the asymptotic limit of small transitions Δa.

This stochastic parametrization follows the same prototype found in previous related studies (Majda et al., 2008). The methodology consists in coupling some simple stochastic triggers (e.g.,

birth/death, spin-flip, coarse-grained lattice models...) to the otherwise deterministic processes, according to some probability laws motivated by physical intuition gained (elsewhere) from observations and detailed numerical simulations (Gardiner, 1994; Katsoulakis et al., 2003; Lawler, 2006). The methodology has been successful in parametrizing with more realism some essential processes of tropical variability for which high irregularity, high intermittency and/or low predictability is involved. This includes applications for the treatment of convective inhibition (Majda and Khouider, 2002; Khouider et al., 2003), of convective momentum transport (Majda and Stechmann, 2008), of the transition from congestus to cumulus to stratiform clouds (Khouider et al., 2010), of the transition to strong convection (Stechmann and Neelin, 2011), or with a realistic Walker-type circulation (Frenkel et al., 2012; Frenkel et al., 2013). Note that while those studies usually focus on parametrizing unresolved mesoscale processes (which are the ones unresolved in GCMs), here we parametrize the unresolved synoptic processes in the skeleton model.

In this article we analyze the dynamics of the stochastic skeleton model in a statistically equilibrated regime. Appendix A details the numerical method used to compute the simulations. The reference parameters values used in this article read, in non-dimensional units: $\overline{Q} = 0.9$, $\Gamma = 1.66$ ($\approx 0.3\,K^{-1}day^{-1}$), $\overline{H} = 0.22$ ($10\,Kday^{-1}$), with stochastic transition parameter $\Delta a = 0.001$. We will consider two experiments that differ by their background states, i.e. by the external sources of cooling/moistening s^θ and s^q. For the experiment described in section 3 those external sources are constant and zonally homogeneous, with values $s^\theta = s^q = 0.022$ ($1\,Kday^{-1}$) at the equator (where we recall that $s^\theta = S^\theta\phi_0$ and $s^q = S^q\phi_0$). For the experiment described in section 4 those external sources are constant yet vary zonally to be representative of a background warm pool state, with values $s^\theta = s^q = 0.022(1 - 0.6\,cos(2\pi x/L))$ at the equator and where L is the equatorial belt length. Such parameter values are consistent with the range of values used in MS2009 and MS2011. In appendix B we briefly summarize some additional sensitivity tests that show the robustness of results to changes in model parameters. In the following sections of this article, simulation results are presented in dimensional units. The dimensional reference scales are x, y: 1500 km, t: 8 hours, u: $50\,m.s^{-1}$, θ, q: 15 K (see table 1 of Stechmann et al., 2008).

3 The stochastic skeleton model with a homogeneous background

In this section, numerical solutions are presented with a homogeneous background state, as represented by the constant and zonally homogeneous external sources of cooling/moistening s^θ and s^q. We analyze the simulations output in the statistically equilibrated regime.

3.1 Power spectra with a homogeneous background

The stochastic skeleton model simulates a MJO-like signal that is the dominant signal at intraseasonal-planetary scale, consistent with observations (Wheeler and Kiladis, 1999). Figure 2 shows the power spectra of the variables as a function of the zonal wavenumber k (in $2\pi/40,000$ km) and frequency ω (in cpd). The MJO appears here as a sharp power peak in the intraseasonal-planetary band ($1 \leq k \leq 5$ and $1/90 \leq \omega \leq 1/30$ cpd), most prominent in u, q and $\overline{Ha}$. This power peak roughly corresponds to the slow eastward phase speed of $\omega/k \approx 5\, ms^{-1}$ with the peculiar relation dispersion $d\omega/dk \approx 0$ found in observations.

This MJO signal results from the internal variability of the stochastic skeleton model: the main generation mechanism is that the MJO mode from linear stability (see figure 1) is excited by the stochastic effects. Indeed, the MJO power peak in figure 2 approximatively matches the dispersion curve of this MJO mode. In addition, it is slightly more prominent in u at wavenumber 1 and in q and $\overline{Ha}$ at wavenumber 5, consistent with the MJO mode eigenvector amplitudes shown in figure 1. Due to the multiplicative stochastic noise and non-linear interactions, there are however some notable differences with the linear solutions. First, the MJO power peak is at slightly lower-frequency than the MJO mode dispersion curve. Second, it also excites weaker power peaks at the double and triple of its frequency (≈ 0.04 cpd and ≈ 0.06 cpd, respectively), which results from the non-linear cross term qa in equation (1) or equation (10).

The other feature at intraseasonal-planetary scale is the power peak near the dispersion curve of the moist Rossby mode from linear stability. This signal is, however, weaker than the MJO signal, as can be seen for example by comparing eastward power (average within $1 \leq k \leq 3$,

$1/90 \leq \omega \leq 1/30$ cpd) and westward power (average within $-3 \leq k \leq -1$, $1/90 \leq \omega \leq 1/30$ cpd) (following e.g. Zhang and Hendon, 1997; Lin et al., 2006). The ratio of eastward/westward power is 3 for u, 5.5 for q, and 2.8 for $\overline{Ha}$, indicating dominant eastward propagations, though it is 0.1 for θ. Note however that θ is weakly associated to the MJO signal in the skeleton model, consistent for example with the weak temperature gradient approximation in the tropics (see the appendix of MS2011; Sobel et al., 2001). There are also power peaks at high-frequencies (≥ 0.08 cpd), most prominent in θ and q, that match well the dispersion curves of the dry Kelvin and dry Rossby modes from linear stability. Finally, recall that various processes found in nature are missing due to the minimal design of the skeleton model, for example the synoptic-scale convectively coupled Kelvin waves that would appear as a power peak around $\omega/k \approx 15\,ms^{-1}$(Wheeler and Kiladis, 1999; Kiladis et al., 2009).

3.2 MJO variability with a homogeneous background

Figure 3 shows the Hovmollers diagrams of the model variables at the equator as well as a data projection e_{MJO} that evaluates the MJO intensity by comparison to other waves from the linear solutions (see MS2011). The data projection, $e_{MJO}(x,t)$, is obtained by filtering all signals to the intraseasonal-planetary band ($1 \leq k \leq 3$, $1/90 \leq \omega \leq 1/30$ cpd), then computing the complex scalar product $e_{MJO}(k,t) = \mathbf{X}_m \mathbf{X}_s^T$ for each wavenumber k and time t from the MJO eigenvector $\mathbf{X}_m(k)$ from linear stability (see figure 1) and the corresponding zonal Fourier series of signals $\mathbf{X}_s(k,t)$, then applying the inverse zonal Fourier transform to $e_{MJO}(k,t)$, with a slight abuse of notation. This representation, along with the other Hovmollers diagrams shown in figure 3, allows us to identify clearly the MJO variability despite the noisy signals. In figure 3 they are some additional large-scale and small-scale propagating structures that are best revealed by computing data projections on other linear solutions (dry Kelvin, dry Rossby, or moist Rossby mode), but those structures do not appear to be directly related to the MJO variability (not shown).

On average, the simulated MJO events propagate eastward with a phase speed of around $5 - 15\,ms^{-1}$ and a roughly constant frequency, consistent with the composite MJO features found in observations. Furthermore, the MJO events are most prominent in u at large scale and couple

to q and $\overline{Ha}$ through a range of smaller scales, consistent with the power spectra shown in figure 2.

The effect of the stochastic fluctuations is to create a realistic intermittency in the simulated MJO. As seen in figure 3 the MJO events are irregular and intermittent, with a great diversity in strength, structure, lifetime and localization. This is an attractive feature of the present stochastic skeleton model in generating MJO variability. In addition, the MJO events are organized into wave trains with growth and demise, i.e. into series of successive MJO events following a primary MJO event, as seen in nature (Matthews, 2008; Yoneyama et al., 2013). One series typically consists of a succession of either two, three, or four MJO events in a row. In figure 3, there is for example a series of four events during the time interval 100-250 days, a series of three events during the time interval 300-450 days, and a series of four events during the time interval 700-900 days. The primary MJO event of a series is sometimes related to a previous series, and sometimes has no particular precursor conditions suggesting that it is spontaneously generated (Matthews, 2008). In addition, each series can be either most prominent at wavenumber 1, wavenumber 2, or both (Hendon and Salby, 1994; Wheeler and Kiladis, 1999).

Figure 4 shows the details of a selected MJO wave train. The MJO propagations with phase speed around $5 - 15\,ms^{-1}$ are clearly visible on u, q, $\overline{Ha}$ and e_{MJO}. It appears visually that the MJO is an envelope of synoptic scale structures, as seen by the smaller scale bursts along the tracks of propagation. This adds to the realism of the simulated MJO, even though the bursts result in part from the superposition of additional small-scale propagations. Note that the oscillations on $\overline{Ha}$ are particularly asymmetric, with sharp and localized maxima: this is expected from the non-linear nature of equation (1) or equation (10) in the skeleton model.

3.3 Interannual variations of the MJO with a homogeneous background

Figure 5(a) shows the magnitude of the data projection e_{MJO} (smoothed over zonal position and time) over a long time interval of 10,000 days. This representation allows us to identify the low-frequency growth and demise of the envelope of each MJO wave train while somewhat filtering out the intraseasonal oscillations associated to individual MJO events. For comparison, the time

interval shown in figure 3 is from 38,200 to 39,200 days.

As seen in figure 5(a), there are marked interannual variations of the MJO that consist of an intermittent alternation between active and inactive low-frequency phases of MJO activity (Hendon et al., 1999). The active low-frequency phases correspond to time intervals with MJO wave trains having a strong intensity (i.e., a strong envelope magnitude), while the inactive low-frequency phases correspond to time intervals with MJO wave trains having a weak intensity (there is, however, always a MJO activity, even weak). There is for example a pronounced inactive phase over the time interval 36,000 to 37,000 days, followed by an active phase over the time interval 37,000 to 38,000 days. This low-frequency modulation of the MJO activity results from the internal variability of the skeleton model alone: indeed the skeleton model here has no prescribed external sources of low-frequency modulation such as for example a seasonal cycle, an El Niño variability, etc (Hendon et al., 1999; Zhang, 2005).

The representation in figure 5(a) also allows us to highlight the overall features of the MJO wave trains, as seen on the evolution of their envelopes. The MJO wave trains show overall slow growth and demise, with however a great diversity in lifetime and intensity. They can be most prominent at wavenumber 1, wavenumber 2, or both. Overall they propagate slowly eastward, while there is visual evidence of some non-propagating standing components (Zhang and Hendon, 1997). In addition, they have no preferred starting location consistent with the background state being zonally homogeneous.

4 The stochastic skeleton model with a warm pool

While the previous section illustrated dynamics with a homogeneous background state, this section illustrates the effect of a background state representative of the equatorial warm pool in nature (see also MS2011). The associated external sources of cooling/moistening s^θ and s^q are shown in figure 6. The warm pool region is centered from $x \approx 10\,000\,km$ to $30\,000\,km$. As in the previous section, we analyze the simulations output in a statistically equilibrated regime. For such a regime the statistical means match the background radiative-convective equilibrium and there is increased convective activity over the warm pool region as seen on the standard deviations of q and $\overline{Ha}$ (not

shown).

The figures 7 to 9 repeat all the diagnostics from previous section with the background warm pool state, while the interannual variations of the MJO are shown in figure 5(b). Overall, the main features of the stochastic skeleton model remain very consistent with the ones presented in previous section for a homogeneous background state, and so they will be described only briefly. The main specific feature with the background warm pool state is that MJO events remain confined to the warm pool region, which is more realistic.

4.1 Power spectra with a warm pool

Figure 7 shows the power spectra of the variables for the simulation with background warm pool state (note that the statistical means have been removed prior to this diagnostic). The dispersion curves from linear stability shown in figure 7 correspond to a homogeneous background state, in order to make easier comparison with figure 2.

The MJO-like signal is the dominant signal at intraseasonal-planetary scale, consistent with observations (Wheeler and Kiladis, 1999). As compared to figure 2 with a homogeneous background state, there is here a slightly increased power at the wavenumbers -1 and 1, consistent with the zonal scale of the background warm pool state. In addition, the power spectra are slightly more blurred, which is likely due to the presence in the skeleton model of two regions (inside and outside the warm pool) with different properties. The ratios of eastward to westward power remain similar: they are here around 2.5 for u, 4.5 for q, 2,5 for $\overline{Ha}$, indicating dominant eastward propagations, and 0.1 for θ.

4.2 MJO variability with a warm pool

Figure 8 shows the Hovmollers diagrams of the variables as well as the data projection e_{MJO} that evaluates the MJO intensity, for the simulation with background warm pool state.

On average, the MJO events propagate eastward with a phase speed of around $5-15\,ms^{-1}$ and a roughly constant frequency, consistent with observations. The effect of the stochastic fluctuations is to create a realistic intermittency in the simulated MJO, with furthermore an organization into

MJO wave trains with growth and demise (Matthews, 2008; Yoneyama et al., 2013). As compared to figure 3 with a homogeneous background state, the MJO events are here confined to the warm pool region, which is more realistic, and they are overall more prominent at wavenumber 1, which is consistent with the zonal scale of the background warm pool state. Similar features were found in MS2011. Most of the MJO events propagate through the entire warm pool region (from $x \approx 10,000$ to $30,000$ km), as seen for example during the time interval 800 to 950 days. However, some of the MJO events propagate through the western warm pool region but stall at the warm pool center corresponding to the maritime continent in nature ($x = 20,000$ km), as seen for example during the time interval 100 to 250 days (Wang and Rui, 1990; Zhang and Hendon, 1997).

Figure 9 shows the details of a selected MJO wave train for the simulation with background warm pool state. The MJO propagations with phase speed around $5 - 15\, ms^{-1}$ are clearly visible for u, q, $\overline{H}a$ and e_{MJO}. This MJO wave train is confined to the warm pool region, though the MJO event at time interval 780-820 days stalls at the warm pool center.

4.3 Interannual variations of the MJO with a warm pool

Figure 5(b) shows the interannual variations of the MJO (i.e., the magnitude of the data projection e_{MJO}) for the simulation with background warm pool state. For comparison, the time interval shown in figure 8 is from 18,800 to 19,800 days.

There are marked interannual variations of the MJO that consist of an intermittent alternation between active and inactive low-frequency phases of MJO activity (Hendon et al., 1999). As compared to figure 5(a) with a homogeneous background state, the MJO activity in figure 5(b) is confined to the warm pool region, which is more realistic. The alternation between active and inactive low-frequency phases of MJO activity is also faster in comparison. As seen in figure 5(b), some MJO wave trains occupy the entire warm pool region (from $x \approx 10,000$ to $30,000$ km), as seen for example at time 15,000 days, while some occupy only the western half (from $x \approx 10,000$ to $20,000$ km), as seen for example during the time interval 11,000 to 12,000 days. Some MJO wave trains occasionally even develop outside the warm pool region.

5 Discussion and Conclusions

We have analyzed the dynamics of a stochastic skeleton model for the MJO. It is a modified version of a minimal dynamical model, the skeleton model, that has been presented in previous work by two of the authors (Majda and Stechmann, 2009b; Majda and Stechmann, 2011). The skeleton model has been shown in previous work to capture together the MJO's salient features of (I) a slow eastward phase speed of roughly $5\,ms^{-1}$, (II) a peculiar dispersion relation with $d\omega/dk \approx 0$, and (III) a horizontal quadrupole structure. In addition to those features, the stochastic skeleton model accounts for some realistic MJO features as seen in nature such as:

IV. The intermittent generation of MJO events, and

V. The organization of MJO events into wave trains with growth and demise.

We have achieved these results by developing a simple stochastic birth/death process for the envelope of synoptic scale activity, that is coupled to otherwise deterministic processes in the skeleton model. The features (I-V) have been recovered in simulations with either a homogeneous background state or a background state representative of the equatorial warm pool, and have been shown to be robust to main parameter changes.

There is an on-going discussion on assessing to which extent the MJO events are generated either as resulting from the internal variability of certain tropical processes or as a secondary response to independently existing extratropical forcings (Zhang, 2005; Lau and Waliser, 2012). Here we contribute to this discussion by showing that (IV) the intermittent generation of MJO events can be accounted for from only the internal variability of a few essential tropical processes such as the ones depicted in the skeleton model. Here, the simulated MJO events are generated spontaneously as resulting from the interaction between the stochastic changes in the level of synoptic activity and the otherwise deterministic planetary processes. Furthermore, this generation is operating with no planetary-scale instability; hence there is also no "scale selection" in the sense of linear instabilities. In fact, as seen in nature, a range of planetary scales is active: wavenumbers 1 and 2 appear prominently for zonal wind, and slightly smaller scales are also prominent for the convective activity. On average, the characteristics of the simulated MJO events are in fair agreement with

the ones of the linear solutions of the skeleton model, but due to their intermittent generation process they further show a great diversity in strength, structure, lifetime and localization.

The stochastic skeleton model presented here simulates MJO events that are (V) organized into wave trains with growth and demise i.e. into series of successive MJO events, either two, three or sometimes more in a row. This feature is qualitatively consistent with the observational record where around 60% of MJO events immediately follow a previous event (Matthews, 2008). During the recent CINDY/DYNAMO field campaign for example, three successive MJO events where observed followed by a pause and an isolated fourth MJO event (Yoneyama et al., 2013; Zhang et al., 2013). In addition, this organization of MJO events into wave trains results in interannual variations of the MJO in the skeleton model, that consist of an intermittent alternation between active and inactive low-frequency phases with enhanced or diminished MJO activity, respectively (Hendon et al., 1999). This low-frequency modulation of the MJO activity results from the internal variability of the skeleton model alone: indeed the skeleton model here has no prescribed external sources of low-frequency modulation such as for example a seasonal cycle, an El Niño variability, etc (Hendon et al., 1999; Zhang, 2005). For a representative background state of convection/heating the MJO wave trains are preferentially confined to the region corresponding to the equatorial warm pool in nature. In particular, some MJO-like disturbances propagate through the western warm pool region but stall at the peak of background convection/heating activity corresponding to the maritime continent in nature (Wang and Rui, 1990; Zhang and Hendon, 1997). As a perspective for future work, the simulation results hint at various plausible mechanisms for the growth and demise of the MJO wave trains. They may be controlled for example by dispersive processes (but not by dissipation), by the stochastic effects, or by the energy transfers from/to the other linear modes of the skeleton model (i.e., the dry Kelvin, dry Rossby, and moist Rossby modes).

While the stochastic skeleton model appears to be a plausible representation of the MJO essential mechanisms, notably with features (I-IV) summarized above, several issues need to be adressed as a perspective for future work. First, one important issue is to find an appropriate observational surrogate for the envelope of synoptic scale wave activity. Secondly, due to it's minimal design the model does not account for several finer details of the MJO's "muscle". These

details include for example refined zonal and vertical structures as well as complex dynamic and convective features within the MJO envelope (e.g., front-to-rear vertical tilts, the vertical structure of westerly wind bursts), the characteristics and intensity of which differ from one MJO event to another (Kikuchi and Takayabu, 2004; Kiladis et al., 2005; Tian et al., 2006; Kiladis et al., 2009). A more complete model should also account for more detailed sub-planetary processes within the MJO's envelope, including for example synoptic-scale convectively coupled waves and/or mesoscale convective systems. This may achieved for example by building suitable stochastic parametrizations, such as the one proposed in the present article, that account for more details of the synoptic and/or mesoscale variability (e.g., Khouider et al., 2010; Frenkel et al., 2012; Frenkel et al., 2013).

Acknowledgments

The research of A. J. M. is partially supported by the Office of Naval Research grant ONR MURI N00014 -12-1-0912. The research of S.N.S. is partially supported by the Office of Naval Research grants ONR YIP N00014-12-1-0744 and ONR MURI N00014-12-1-0912. S.T. is supported as a postdoctoral fellow through A.J.M's ONR MURI grant.

Appendix

A. Numerical Method

This appendix details the numerical method used to compute the simulations. The stochastic skeleton model is the vertically and meridionally truncated system of variables K, R, Q, A from equation (4), where the non-linear amplitude equation is replaced by the stochastic birth/death process from equation (9). In practice, we however solve a more suitable system of variables K, R, Z, a, where we introduce the new variable $Z = q + \overline{Q}\theta$. To remain consistent with the notations from both section 2.1 and 2.2, consider here that the variables q, θ, a (and Z) are defined in a zonal strip along the equator, with $q = q(x, 0, t)$, $\theta = \theta(x, 0, t)$ and $a = a(x, 0, t)$. Therefore, we have $q = Q\phi_0(0)$, $\theta = -[K + R]\phi_0(0)$ and $a = A\phi_0(0)$ for consistency with equations (4). In addition, we recall that $a = \Delta a\, \eta$ for consistency with equations (9).

All model variables K, R, Z, a are random variables, and we solve for the evolution of one model realization. The spatial and temporal resolution is identical to MS2011, with a spatial step Δx of 625 km spanning the equatorial belt (40,000 km) and a timestep ΔT of around 1.7 hours. We use a splitting method to update the system over each timestep ΔT. First, Z and a in the zonal strip are held fixed and we solve for the evolution of K and R exactly using zonal Fourier series (cf. first and second rows of equation (4)). Second, K and R are held fixed and we solve for the evolution of Z and a together. For this, we solve a local system of equations:

$$\begin{aligned} \partial_t Z &= (1-\overline{Q})(s^q - \overline{H}a) \\ a(t+\tau) &= a(t) + \xi \Delta a \,. \end{aligned} \tag{13}$$

The first row of equation (13) can be deduced by combining the third and fourth rows of equation (3), or alternatively the three first rows of equation (4). The second row of equation (13) ensues when solving one realization of the master equation (9) (see below). Here, the equation (13) is solved over each timestep ΔT as a series of consecutive transitions over smaller timesteps τ (where τ as well as ξ are recomputed after each consecutive transition). The last consective transition in particular usually occurs after the end of the timestep ΔT, and is therefore approximatively omitted in order to retrieve $Z(t+\Delta T)$ and $a(t+\Delta T)$.

The second row of equation (13) ensues when solving one realization of the master equation (9) with the Gillespie algorithm (Gillespie, 1975; Gillespie, 1977). This consists in updating a sequentially according to the random variables τ and ξ. Here, $\tau \geq 0$ is the random time interval between two consecutive transitions, with cumulative distribution function $P(\tau) = \exp(-(\lambda+\mu)\tau)$ that corresponds to a Poisson distribution. This depends on the transition rates λ and μ given earlier in equation (11). In addition, ξ is the transition direction, and it takes the discrete values $\{-1, 1\}$ according to the cumulative distribution function $P(\xi) = \{\mu/(\lambda+\mu), \lambda/(\lambda+\mu)\}$. For the transitions rates given in equation (11), $\xi = 1$ if $q \geq 0$ and $\xi = -1$ if $q < 0$ (though $\xi = 1$ unconditionnaly if $a = 0$), which is consistent with equation (1). In other words, the main stochastic effect in the second row of equation (13) is that the growth/decay of the envelope of synoptic activity a can be randomly enhanced or diminished as compared to the otherwise

deterministic equation (1).

In this article we analyze the dynamics of the stochastic skeleton model in a statistically equilibrated regime. The statistically equilibrated regime is reached after around 10,000 days of simulations, after an initial growth in oscillation amplitude. The simulations are initiated from the radiative-convective equilibrium state plus an initial perturbation, as in MS2011. Due to the stochastic effects, the choice of the initial perturbation has no impact on the statistically equilibrated regime, yet this allows us to "start" the stochastic fluctuations because it sets $\lambda \neq 0$ and $\mu \neq 0$. This model is inexpensive computationally: 1000 days of simulation take around 2 minutes of computer time on a typical laptop computer.

B. Sensitivity to Parameters

The main features of the stochastic skeleton model are overall robust to parameter changes, as shown here with a few sensitivity tests (see also section 2.2 for the reference values). While the previous sections illustrated dynamics with stochastic transition parameter $\Delta a = 10^{-3}$, we have also analyzed additional simulations with $\Delta a = 10^{-4}$ and $\Delta a = 10^{-5}$. The robustness of results is briefly illustrated in figure 10 that shows the power spectra of u. For all simulations, the MJO signal is the dominant signal at intraseasonal-planetary scale and it appears as a sharp power peak slightly under the dispersion curve of the MJO mode from linear stability. For the simulations with background warm pool state there is furthermore a slightly increased power at wavenumber -1 and 1. Those results are consistent with the ones from previous sections. We have also found overall consistent results in additional simulations with an intermediate warm pool strength, and in simulations with modified parameter $\Gamma/2$ or 2Γ like in MS2009 (not shown).

References

Biello, J. A. and Majda, A. J. (2005). A New Multiscale Model for the Madden-Julian Oscillation. *J. Atmos. Sci.*, 62(6):1694–1721.

595 Dias, J., Leroux, S., Tulich, S. N., and Kiladis, G. N. (2013). How systematic is organized tropical
596 convection within the MJO? *Geophys. Res. Lett.*, 40:1420–1425.

597 Frenkel, Y., Majda, A. J., and Khouider, B. (2012). Using the Stochastic Multicloud Model to
598 Improve Tropical Convective Parameterization: A Paradigm Example. *J. Atmos. Sci.*, 69:1080–
599 1105.

600 Frenkel, Y., Majda, A. J., and Khouider, B. (2013). Stochastic and Deterministic Multicloud
601 parameterizations for tropical convection. *Climate Dyn.*, doi:10.1007/s00382-013-1678-z.

602 Gardiner, C. W. (1994). *Handbook of stochastic methods for physics, chemistry, and the natural*
603 *sciences*. Springer. 442pp.

604 Gill, A. (1980). Some simple solutions for heat-induced tropical circulation. *Quart. J. Roy. Meteor.*
605 *Soc.*, 106:447–462.

606 Gillespie, D. T. (1975). An Exact Method for Numerically Simulating the Stochastic Coalescence
607 Process in a Cloud. *J. Atmos. Sci.*, 32:1977–1989.

608 Gillespie, D. T. (1977). Exact Stochastic Simulation of Coupled Chemical Reactions. *J. Phys.*
609 *Chem.*, 81(25):2340–2361.

610 Grabowski, W. (2001). Coupling processes with the large-scale dynamics using the cloud-resolving
611 convection parametrization (CRCP). *J. Atmos. Sci.*, 58:978–997.

612 Grabowski, W. W. and Moncrieff, M. W. (2004). Moisture-convection feedback in the Tropics.
613 *Quart. J. Roy. Meteor. Soc.*, 130:3081–3104.

614 Hendon, H. H. and Liebmann, B. (1994). Organization of convection within the Madden-Julian
615 oscillation. *J. Geophys. Res.*, 99:8073–8083.

616 Hendon, H. H. and Salby, M. L. (1994). The Life Cycle of the Madden-Julian Oscillation. *J.*
617 *Atmos. Sci.*, 51:2225–2237.

618 Hendon, H. H., Zhang, C., and Glick, J. (1999). Interannual Variation of the Madden-Julian
619 Oscillation during Austral Summer. *J. Climate*, 12:2538–2550.

620 Holloway, C. E. and Neelin, J. D. (2009). Moisture Vertical Structure, Column Water Vapor, and
621 Tropical Deep Convection. *J. Atmos. Sci.*, 66:1665–1683.

622 Katsoulakis, M. A., Majda, A. J., and Vlachos, D. G. (2003). Coarse-grained stochastic processes
623 for microscopic lattice systems. *Proc. Natl. Acad. Sci. USA*, 100(3):782–787.

624 Khouider, B., Biello, J. A., and Majda, A. J. (2010). A Stochastic Multicloud Model for Tropical
625 Convection. *Comm. Math. Sci.*, 8(1):187–216.

626 Khouider, B. and Majda, A. J. (2006). A simple multicloud parametrization for convectively
627 coupled tropical waves. Part I: Linear Analysis. *J. Atmos. Sci.*, 63:1308–1323.

628 Khouider, B. and Majda, A. J. (2007). A Simple Multicloud Parameterization for Convectively
629 Coupled Tropical Waves. Part II: Nonlinear Simulations. *J. Atmos. Sci.*, 64:381–400.

630 Khouider, B., Majda, A. J., and Katsoulakis, M. A. (2003). Coarse-grained stochastic models for
631 tropical convection and climate. *Proc. Natl. Acad. Sci.*, 100(21):11941–11946.

632 Khouider, B., St-Cyr, A., Majda, A. J., and Tribbia, J. (2011). The MJO and Convectively
633 Coupled Waves in a Coarse-Resolution GCM with a Simple Multicloud Parametrization. *J.*
634 *Atmos. Sci.*, 68:240–264.

635 Kikuchi, K. and Takayabu, Y. N. (2004). The development of organized convection associated
636 with the MJO during TOGA COARE IOP: Trimodal characteristics. *Geophys. Res. Lett.*, 31.
637 L10101,doi:10.1029/2004GL019601.

638 Kiladis, G. N., Straub, K. H., and T., H. P. (2005). Zonal and vertical structure of the Madden-
639 Julian oscillation. *J Atmos Sci*, 62:2790–2809.

640 Kiladis, G. N., Wheeler, C., Haertel, P. T., Straub, K. H., and Roundy, P. E. (2009). Convectively
641 coupled equatorial waves. *Rev. Geophys.*, 47. RG2003, doi:10.1029/2008RG000266.

642 Kim, D., K., S., Stern, W., Waliser, D., Kang, I.-S., Maloney, E., Wang, W., Weickmann, K.,
643 Benedict, J., Khairoutdinov, M., Lee, M.-I., Neale, R., Suarez, M., Thayer-Calder, K., and

644 Zhang, G. (2009). Application of MJO simulation diagnostics to climate models. *J. Climate*,
645 22:6413–6436.

646 Lau, W. M. and Waliser, D. E. (2012). *Intraseasonal Variability in the Atmosphere-Ocean Climate*
647 *System*. Springer. 642pp.

648 Lawler, G. F. (2006). *Introduction to Stochastic Processes*. Chapman and Hall/CRC. 192pp.

649 Lin, J.-L., Kiladis, G. N., Mapes, B. E., Weickmann, K. M., Sperber, K. R., Lin, W., Wheeler,
650 M. C., Schubert, S. D., Del Genio, A., Donner, L. J., Emori, S., Gueremy, J.-F., Hourdin, F.,
651 Rasch, P. J., Roeckner, E., and Scinocca, J. F. (2006). Tropical Intraseasonal Variability in 14
652 IPCC AR4 Climate Models. Part I: Convective Signals. *J. Climate*, 19:2665–2690.

653 Liu, F. and Wang, B. (2012). A Frictional Skeleton Model for the Madden-Julian Oscillation. *J.*
654 *Atmos. Sci.*, 69:2749–2758.

655 Madden, R. E. and Julian, P. R. (1971). Detection of a 40-50 day oscillation in the zonal wind in
656 the tropical Pacific. *J. Atmos. Sci.*, 28:702–708.

657 Madden, R. E. and Julian, P. R. (1994). Observations of the 40-50 day tropical oscillation-A
658 review. *Mon. Wea. Rev.*, 122:814–837.

659 Majda, A. J. (2003). *Introduction to PDEs and Waves for the Atmosphere and Ocean. Courant*
660 *Lecture Notes in Mathematics, Vol 9.* American Mathematical Society. Providence, x+234pp.

661 Majda, A. J. and Biello, J. A. (2004). A multiscale model for tropical intraseasonal oscillations.
662 *Proc. Natl. Acad. Sci. USA*, 101:4736–4741.

663 Majda, A. J., Franzke, C., and Khouider, B. (2008). An applied mathematics perspective on
664 stochastic modelling for climate. *Philosophical Transactions of the Royal Society A: Mathemat-*
665 *ical, Physical and Engineering Sciences*, 366(1875):2427–2453.

666 Majda, A. J. and Khouider, B. (2002). Stochastic and mesoscopic models for tropical convection.
667 *Proc. Natl. Acad. Sci.*, 99:1123–1128.

668 Majda, A. J. and Stechmann, S. N. (2008). Stochastic models for convective momentum transport.
669 *Proc. Natl. Acad. Sci. USA*, 105(46):17614–17619.

670 Majda, A. J. and Stechmann, S. N. (2009a). A Simple Dynamical Model with Features of Con-
671 vective Momentum Transport. *J. Atmos. Sci.*, 66:373–392.

672 Majda, A. J. and Stechmann, S. N. (2009b). The skeleton of tropical intraseasonal oscillations.
673 *Proc. Natl. Acad. Sci.*, 106:8417–8422.

674 Majda, A. J. and Stechmann, S. N. (2011). Nonlinear Dynamics and Regional Variations in the
675 MJO Skeleton. *J. Atmos. Sci.*, 68:3053–3071.

676 Majda, A. J., Stechmann, S. N., and Khouider, B. (2007). Madden-Julian oscillation analog and
677 intraseasonal variability in a multicloud model above the equator. *Proc. Natl. Acad. Sci. USA*,
678 104:9919–9924.

679 Matsuno, T. (1966). Quasi-geostrophic motions in the equatorial area. *J. Meteor. Soc. Japan*,
680 44:25–43.

681 Matthews, A. J. (2008). Primary and successive events in the Madden-Julian Oscillation. *Quart.*
682 *J. Roy. Meteor. Soc.*, 134:439–453.

683 Moncrieff, M. (2004). Analytic representation of the large-scale organization of tropical convection.
684 *Quart. J. Roy. Meteor. Soc.*, 130:1521–1538.

685 Moncrieff, M. W., Shapiro, M., Slingo, J., and Molteni, F. (2007). Collaborative research at the
686 intersection of weather and climate. *WMO Bull.*, 56:204–211.

687 Palmer, T. N. (2012). Towards the probabilistic Earth-system simulator: a vision for the future of
688 climate and weather prediction. *Quart. J. Roy. Meteor. Soc.*, 138:841–861.

689 Raymond, D. J. (2001). A New Model of the Madden-Julian Oscillation. *J. Atmos. Sci.*, 58:2807–
690 2819.

691 Sobel, A. H., Nilsson, J., and Polvani, L. M. (2001). The Weak Temperature Gradient Approxi-
692 mation and Balanced Tropical Moisture Waves. *J. Atmos. Sci.*, 58:3650–3665.

693 Stechmann, S., Majda, A. J., and Skjorshammer, D. (2013). Convectively coupled wave-
694 environment interactions. *Theor. Comp. Fluid Dyn.*, 27, Issue 3-4:513–532.

695 Stechmann, S. N., Majda, A. J., and Boulaem, K. (2008). Nonlinear Dynamics of Hydrostatic
696 Internal Gravity Waves. *Theor. Comp. Fluid Dyn.*, 22, Issue 6:407–432.

697 Stechmann, S. N. and Neelin, J. D. (2011). A Stochastic Model for the Transition to Strong
698 Convection. *J. Atmos. Sci.*, 68:2955–2970.

699 Straub, K. (2013). MJO Initiation in the Real-Time Multivariate MJO Index. *J. Climate*, 26:1130–
700 1151.

701 Tian, B., Waliser, D., Fetzer, E., Lambrigsten, B., Yung, Y., and Wang, B. (2006). Vertical moist
702 thermodynamic structure and spatial-temporal evolution of the MJO in AIRS observations. *J.*
703 *Atmos. Sci.*, 63:2462–2485.

704 Wang, B. and Liu, F. (2011). A Model for Scale Interaction in the Madden-Julian Oscillation. *J.*
705 *Atmos. Sci.*, 68:2524–2536.

706 Wang, B. and Rui, H. (1990). Synoptic Climatology of Transient Tropical Intraseasonal Convection
707 Anomalies: 1975-1985*. *Meteorol. Atmos. Phys.*, 44:43–61.

708 Wheeler, M. and Kiladis, G. N. (1999). Convectively Coupled Equatorial Waves: Analysis of
709 Clouds and Temperature in the Wavenumber-Frequency Domain. *J. Atmos. Sci.*, 56:374–399.

710 Yoneyama, K., Zhang, C., and Long, C. N. (2013). Tracking Pulses of the Madden-Julian Oscilla-
711 tion. *Bull. Am. Meteor. Soc.* ,doi: http://dx.doi.org/10.1175/BAMS-D-12-00157.1, in press.

712 Zhang, C. (2005). Madden-Julian Oscillation. *Reviews of Geophysics*, 43. RG2003,
713 doi:10.1029/2004RG000158.

714 Zhang, C., Gottschalck, J., Maloney, E. D., Moncrieff, M. W., Vitart, F., Waliser, D. E., Wang, B.,
715 and Wheeler, M. C. (2013). Cracking the MJO nut. *Geophys. Res. Lett.*, 40, Issue 6:1223–1230.

716 Zhang, C. and Hendon, H. H. (1997). Propagating and standing components of the intraseasonal
717 oscillation in tropical convection. *J. Atmos. Sci.*, 54:741–752.

Figure Captions

Figure 1: Summary of the skeleton model linear stability: (a) phase speed ω/k $(m.s^{-1})$, (b) frequency ω (cpd), and (c) component amplitudes of the eigenvector $\mathbf{X}_m(k) = [K, R, Q, A]$, as a function of the zonal wavenumber k $(2\pi/40000km)$. The black circles mark the integer wavenumbers satisfying periodic boundary conditions. This is repeated for each eigenmode, from top to bottom in order of decreasing phase speed: (a)(b)(c) dry Kelvin mode, (d)(e)(f) MJO mode, (h)(i)(j) moist Rossby mode, and (k)(l)(m) dry Rossby mode.

Figure 2: Zonal wavenumber-frequency power spectra (with homogeneous background): For (a) u (ms^{-1}), (b) θ (K), (c) q (K), and (d)$\overline{Ha}$ $(Kday^{-1})$ taken at the equator, as a function of zonal wavenumber (in $2\pi/40000km$) and frequency (cpd). The contour levels are in the base 10-logarithm, for the dimensional variables taken at the equator. The black circles mark the dispersion curves from linear stability as in figure 1. The black dashed lines mark the periods 90 and 30 days.

Figure 3: Hovmoller diagrams (with homogeneous background): for (a) u $(m.s^{-1})$, (b) θ (K), (c) q (K), and (d) $\overline{Ha}$ $(K.day^{-1})$ at the equator, as well as (e) the data projection e_{MJO}, as a function of zonal location x (in 1000 km) and time (in days from a reference time at 38,200 days).

Figure 4: Hovmollers diagrams (with homogeneous background), zoomed on the time interval 70-270 days from figure 3: for (a) u $(m.s^{-1})$, (b) θ (K), (c) q (K), and (d) $\overline{Ha}$ $(K.day^{-1})$ at the equator, as well as (e) the data projection e_{MJO}, as a function of zonal location x (in 1000 km) and time t (in days from a reference time at 38,200 days).

Figure 5: Interannual variations of the MJO: Hovmoller diagram of the magnitude of the data projection e_{MJO}, as a function of zonal location x (1000 km) and time t (in 1000 days from the simulation beginning). This is for (a) the simulation with a homogeneous background state, and (b) the simulation with a background warm pool state. The data are smoothed 5 times with a 3000km by 20 day box kernel.

Figure 6: Zonal shape of the background warm pool state: $s^\theta = s^q$ $(Kday^{-1})$ at the equator as a function of zonal location x (1000 km).

Figure 7: Zonal wavenumber-frequency power spectra (with warm pool): For (a) u (ms^{-1}), (b) θ (K), (c) q (K), and (d)$\overline{H}a$ ($Kday^{-1}$), as a function of zonal wavenumber (in $2\pi/40000km$) and frequency (in cpd). The contour levels are in the base 10-logarithm, for the dimensional variables taken at the equator. The black circles mark the dispersion curves from linear stability as in figure 1. The black dashed lines mark the periods 90 and 30 days.

Figure 8: Hovmoller diagrams (with warm pool): for (a) u ($m.s^{-1}$), (b) θ (K), (c) q (K), and (d) $\overline{H}a$ ($K.day^{-1}$) at the equator, as well as (e) the data projection e_{MJO}, as a function of zonal location x (in 1000 km) and time t (in days from a reference time at 18,800 days).

Figure 9: Hovmoller diagrams with (warm pool), zoomed on the time interval 770-970 days from figure 8: for (a) u ($m.s^{-1}$), (b) θ (K), (c) q (K), and (d) $\overline{H}a$ ($K.day^{-1}$) at the equator, as well as (e) the data projection e_{MJO}, as a function of zonal location x (1000 km) and time t (in days from a reference time at 18,800 days).

Figure 10: Sensitivity to Δa: Zonal wavenumber-frequency power spectra of u, for (a) $\Delta a = 10^{-5}$, (b) $\Delta a = 10^{-4}$, and (c) $\Delta a = 10^{-3}$, as a function of zonal wavenumber (in $2\pi/40000km$) and frequency (in cpd), for simulations with a homogeneous background state. (d)(e)(f) repeats the graphs for simulations with background warm pool state. Figure setup is identical to the one of figure 2 and figure 7.

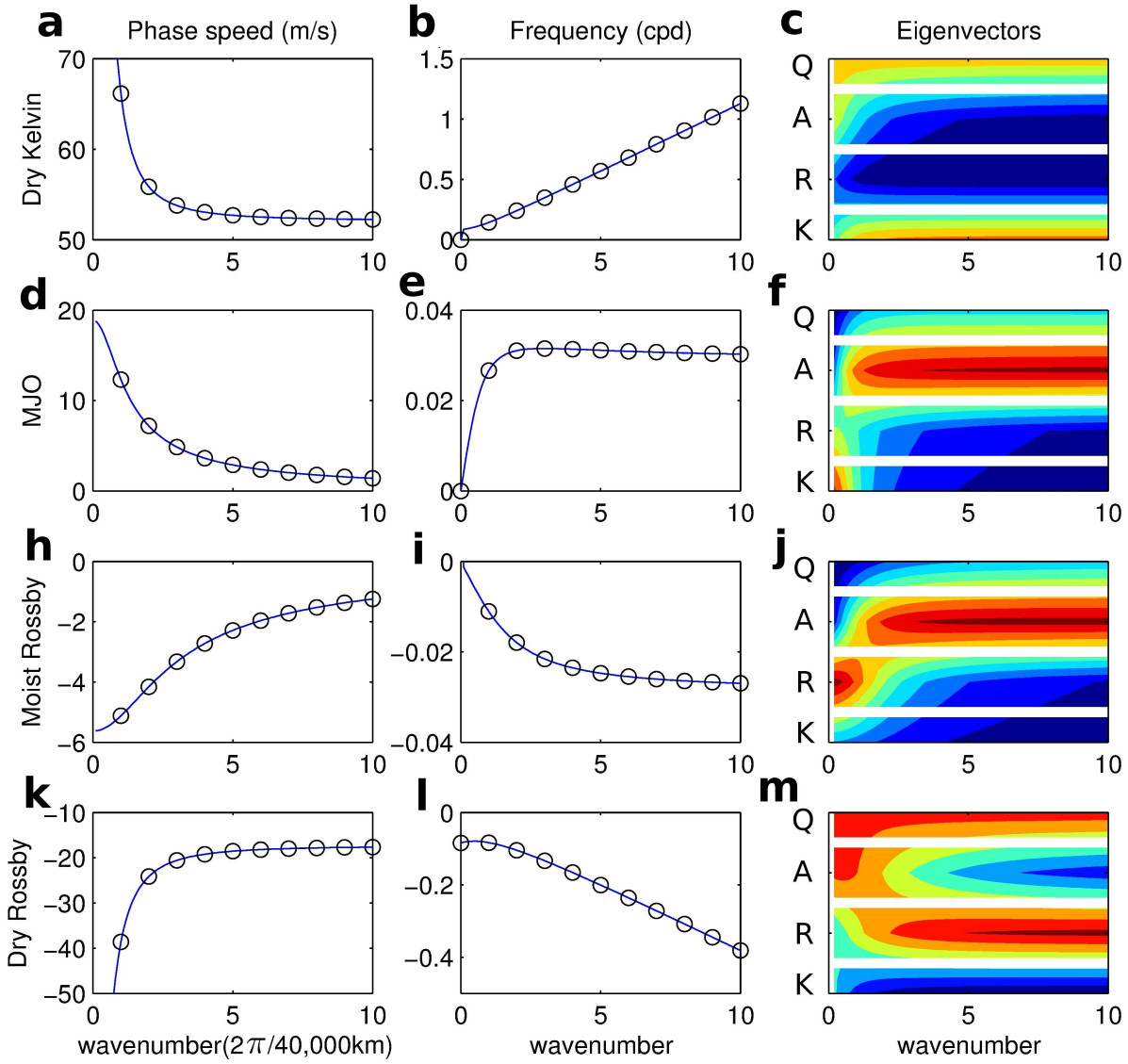

Figure 1: Summary of the skeleton model linear stability: (a) phase speed ω/k $(m.s^{-1})$, (b) frequency ω (cpd), and (c) component amplitudes of the eigenvector $\mathbf{X}_m(k) = [K, R, Q, A]$, as a function of the zonal wavenumber k $(2\pi/40000km)$. The black circles mark the integer wavenumbers satisfying periodic boundary conditions. This is repeated for each eigenmode, from top to bottom in order of decreasing phase speed: (a)(b)(c) dry Kelvin mode, (d)(e)(f) MJO mode, (h)(i)(j) moist Rossby mode, and (k)(l)(m) dry Rossby mode. .

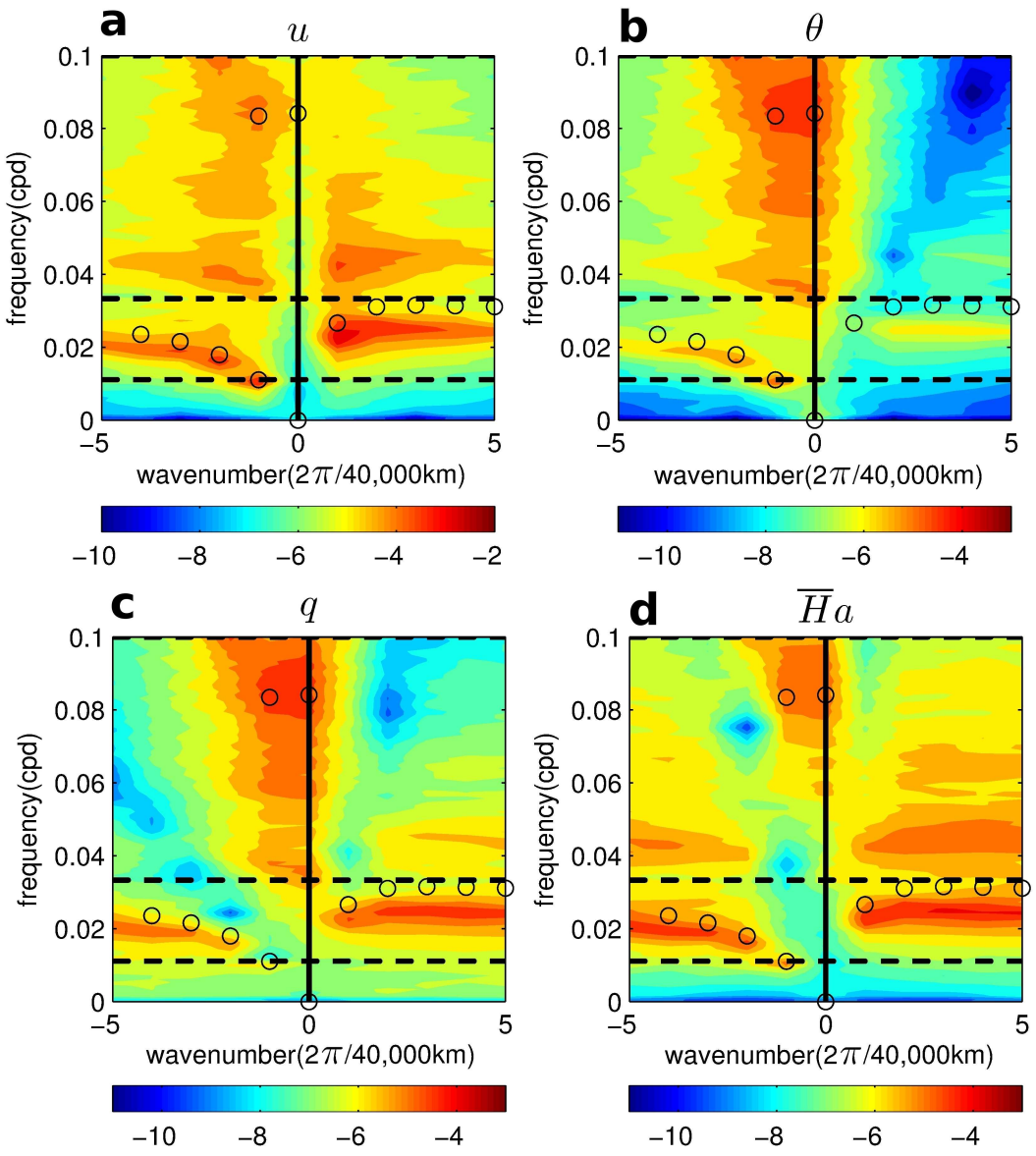

Figure 2: Zonal wavenumber-frequency power spectra (with homogeneous background): For (a) u (ms^{-1}), (b) θ (K), (c) q (K), and (d)$\overline{Ha}$ $(Kday^{-1})$ taken at the equator, as a function of zonal wavenumber (in $2\pi/40000km$) and frequency (cpd). The contour levels are in the base 10-logarithm, for the dimensional variables taken at the equator. The black circles mark the dispersion curves from linear stability as in figure 1. The black dashed lines mark the periods 90 and 30 days..

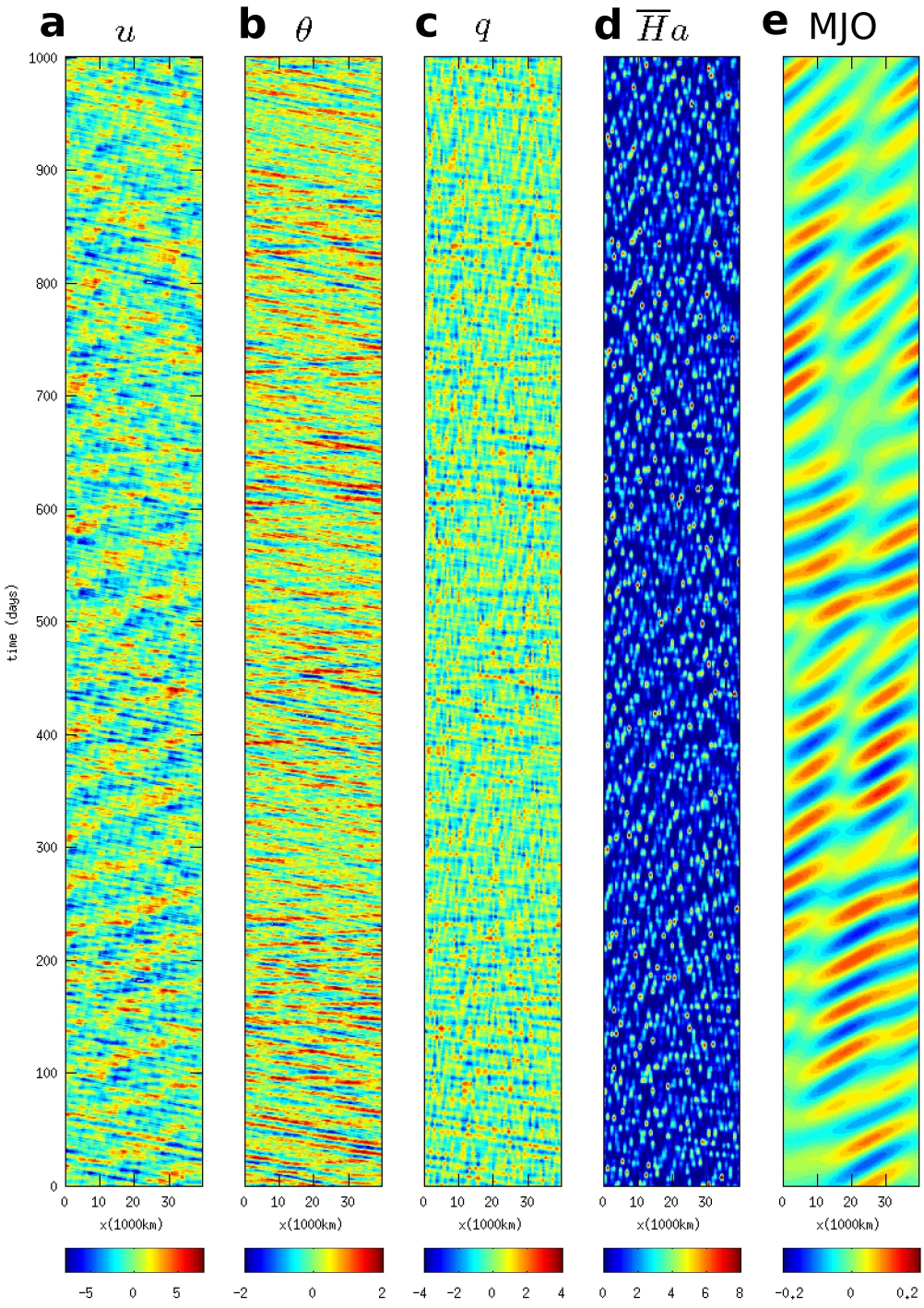

Figure 3: Hovmoller diagrams (with homogeneous background): for (a) u $(m.s^{-1})$, (b) θ (K), (c) q (K), and (d) $\overline{H}a$ $(K.day^{-1})$ at the equator, as well as (e) the data projection e_{MJO}, as a function of zonal location x (in 1000 km) and time (in days from a reference time at 38,200 days).

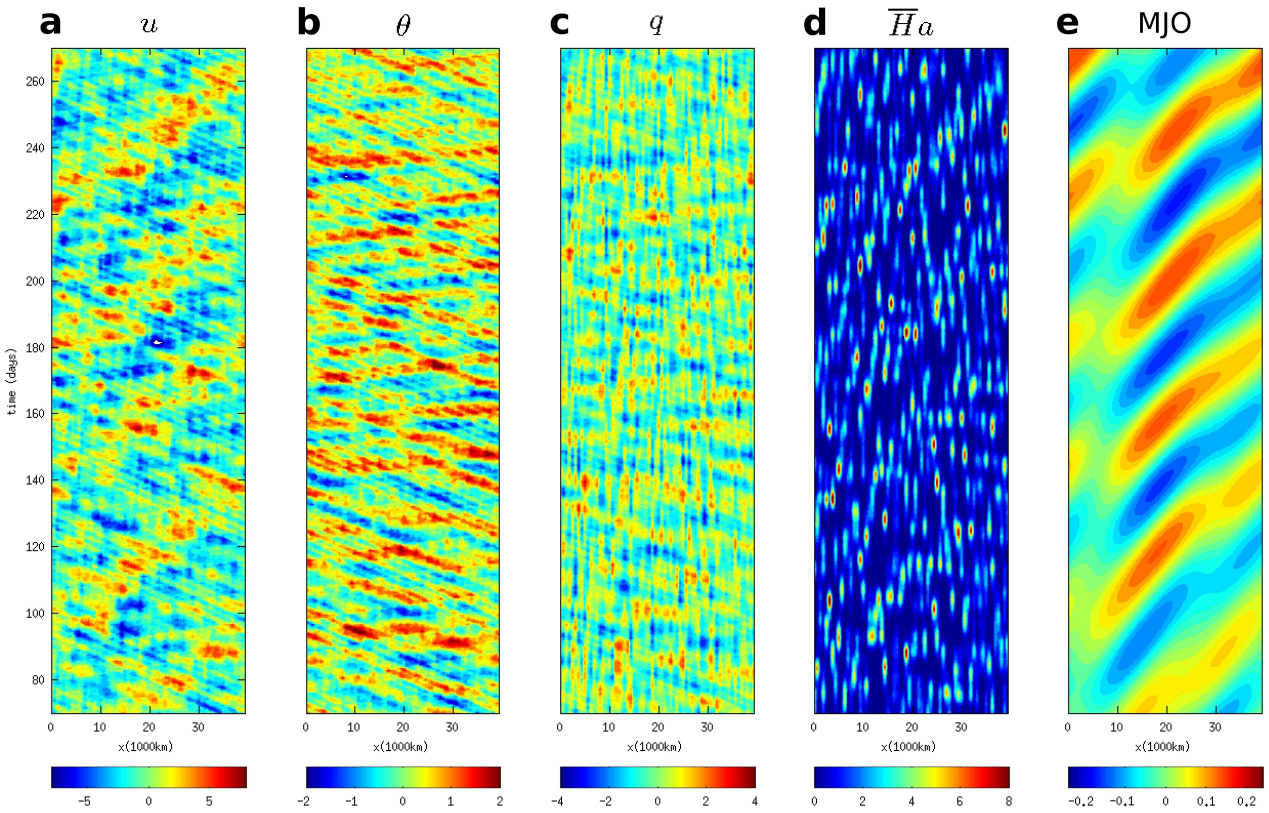

Figure 4: Hovmollers diagrams (with homogeneous background), zoomed on the time interval 70-270 days from figure 3: for (a) u $(m.s^{-1})$, (b) θ (K), (c) q (K), and (d) $\overline{H}a$ $(K.day^{-1})$ at the equator, as well as (e) the data projection e_{MJO}, as a function of zonal location x (in 1000 km) and time t (in days from a reference time at 38,200 days).

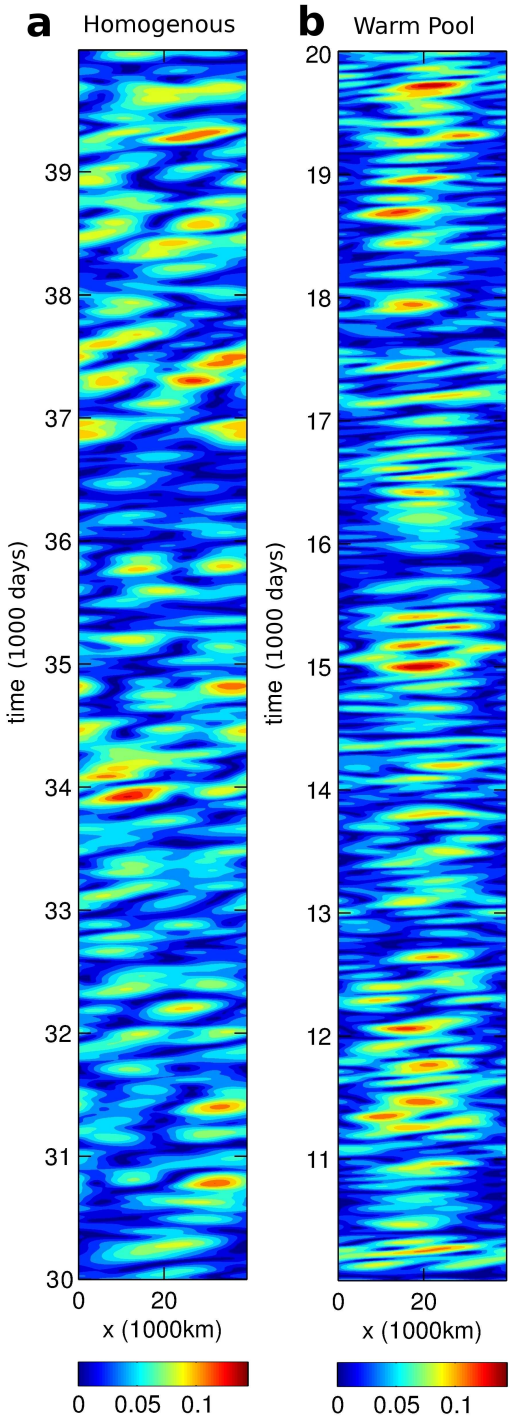

Figure 5: Interannual variations of the MJO: Hovmoller diagram of the magnitude of the data projection e_{MJO}, as a function of zonal location x (1000 km) and time t (in 1000 days from the simulation beginning). This is for (a) the simulation with a homogeneous background state, and (b) the simulation with a background warm pool state. The signals are smoothed 5 times with a 3000km by 20 day box kernel.

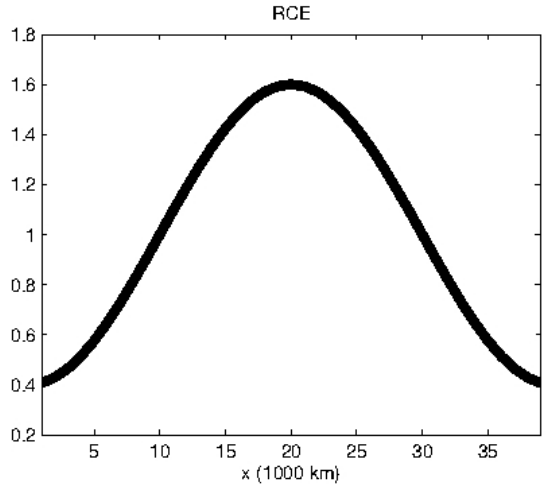

Figure 6: Zonal shape of the background warm pool state: $s^{\theta} = s^{q}$ $(Kday^{-1})$ at the equator as a function of zonal location x (1000 km).

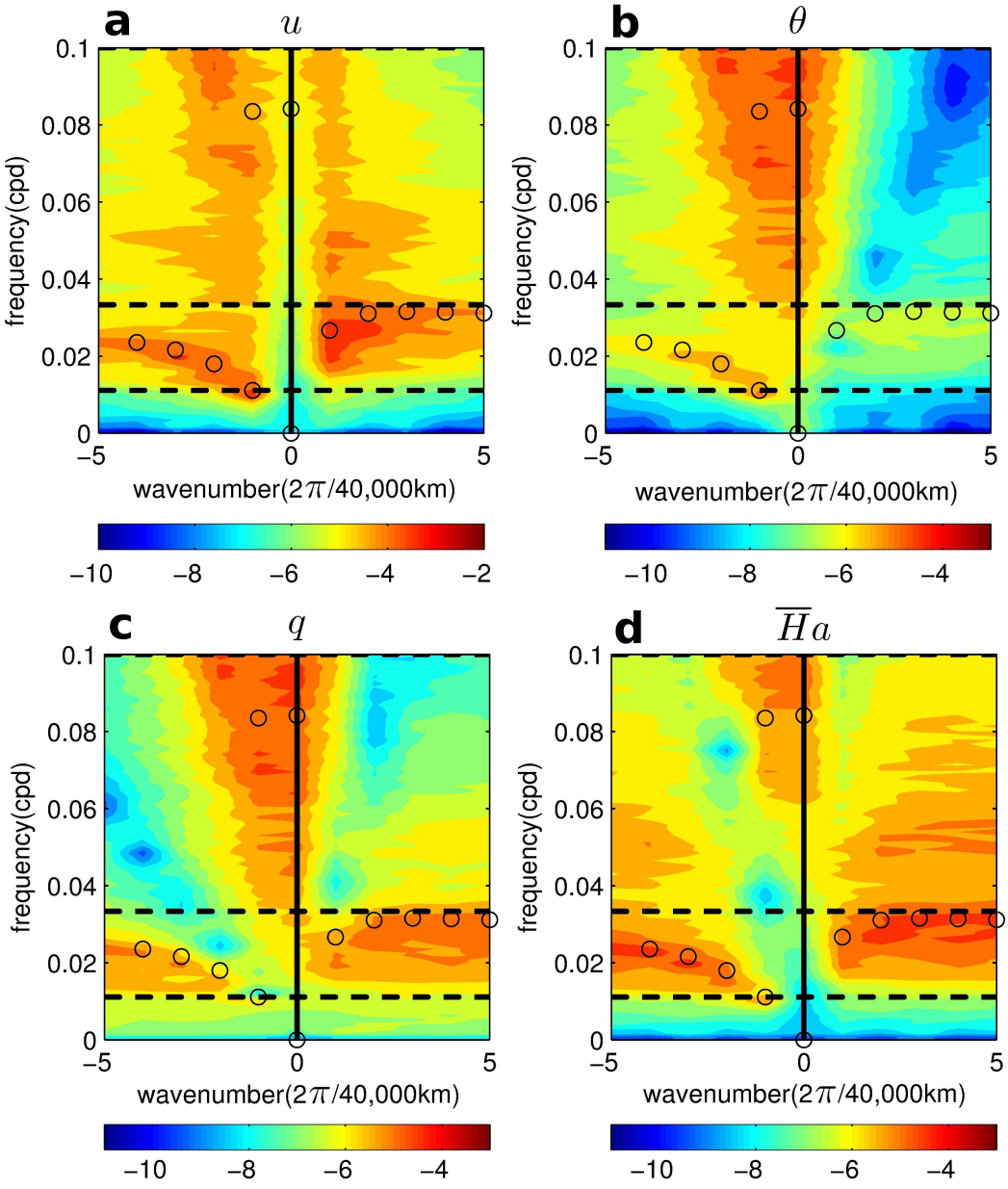

Figure 7: Zonal wavenumber-frequency power spectra (with warm pool): For (a) u (ms^{-1}), (b) θ (K), (c) q (K), and (d)$\overline{H}a$ $(Kday^{-1})$, as a function of zonal wavenumber (in $2\pi/40000km$) and frequency (in cpd). The contour levels are in the base 10-logarithm, for the dimensional variables taken at the equator. The black circles mark the dispersion curves from linear stability as in figure 1. The black dashed lines mark the periods 90 and 30 days.

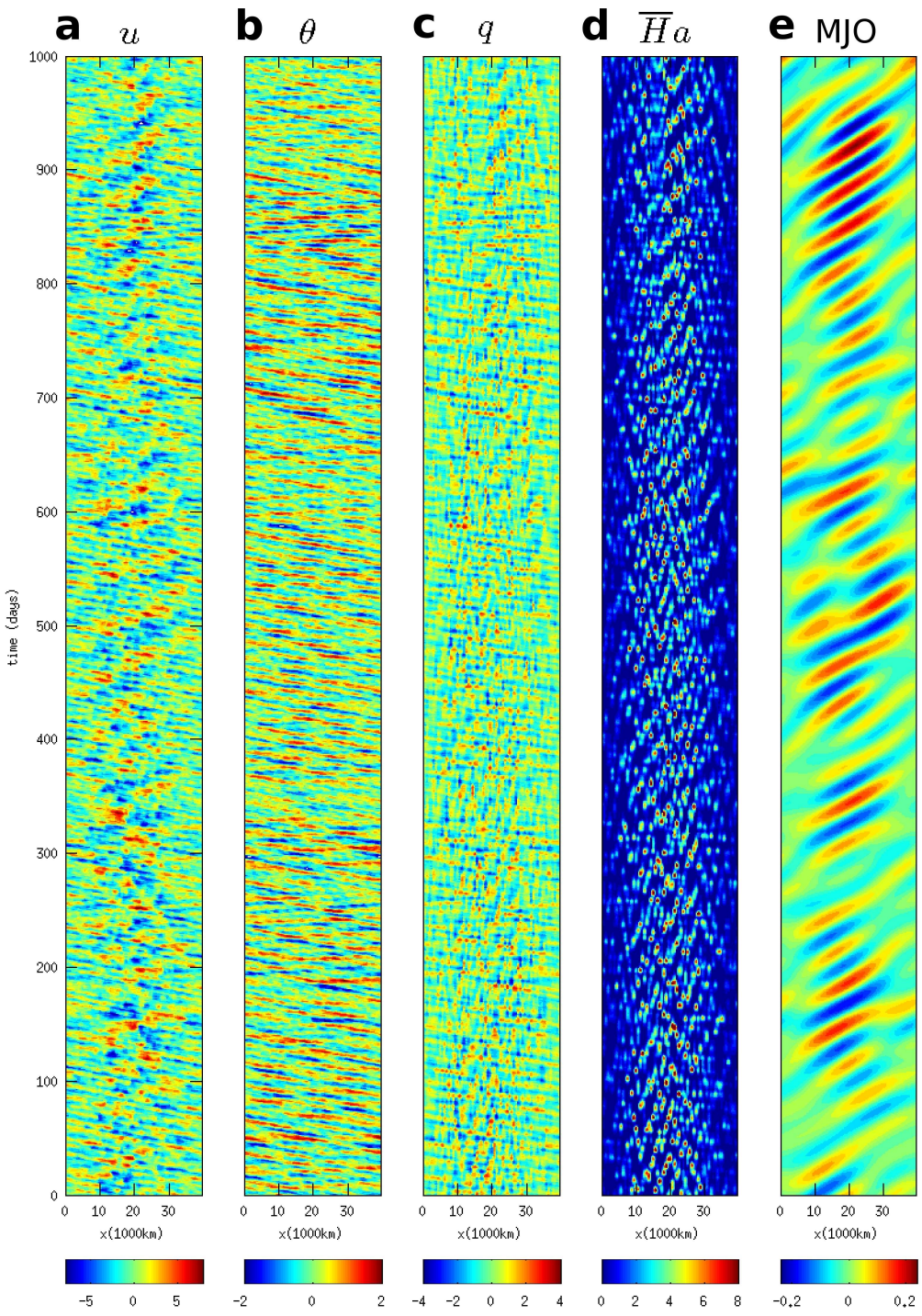

Figure 8: Hovmoller diagrams (with warm pool): for (a) u $(m.s^{-1})$, (b) θ (K), (c) q (K), and (d) $\overline{H}a$ $(K.day^{-1})$ at the equator, as well as (e) the data projection e_{MJO}, as a function of zonal location x (in 1000 km) and time t (in days from a reference time at 18,800 days).

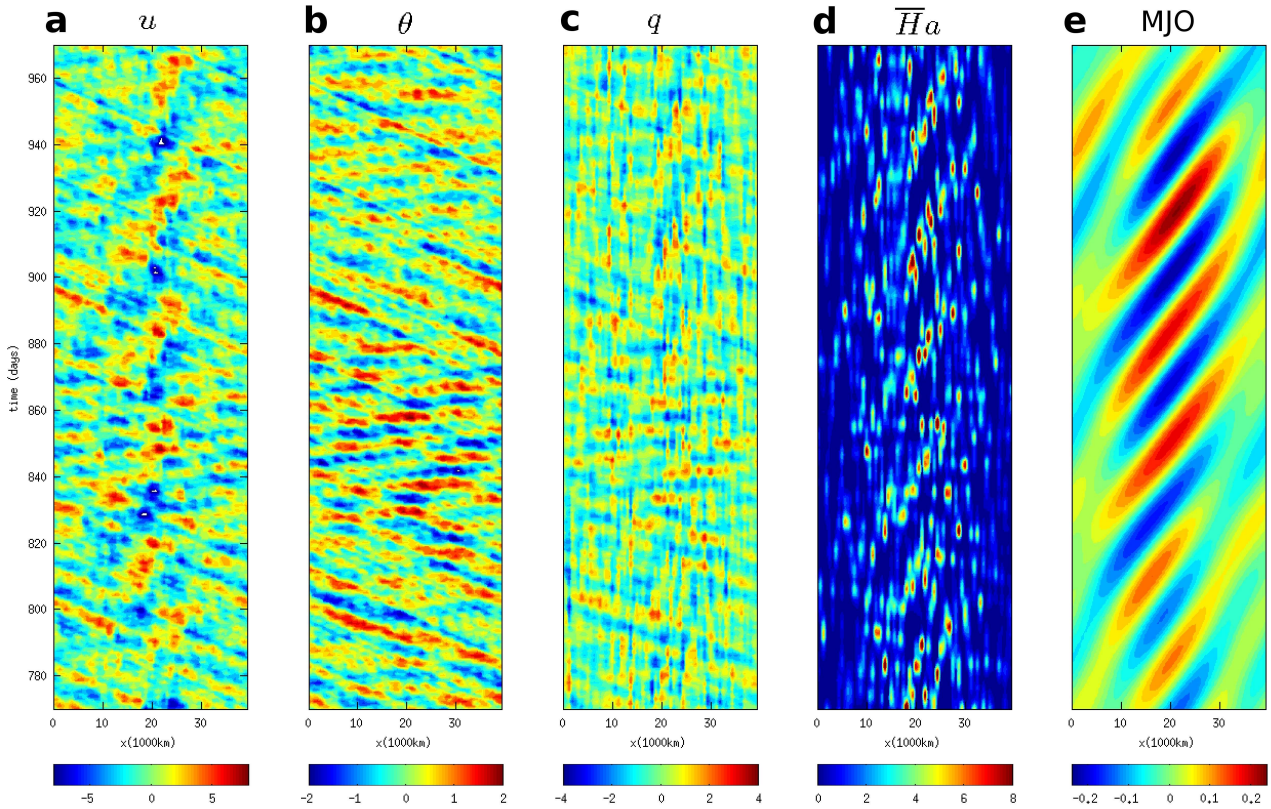

Figure 9: Hovmoller diagrams with (warm pool), zoomed on the time interval 770-970 days from figure 8: for (a) u $(m.s^{-1})$, (b) θ (K), (c) q (K), and (d) $\overline{H}a$ $(K.day^{-1})$ at the equator, as well as (e) the data projection e_{MJO}, as a function of zonal location x (1000 km) and time t (in days from a reference time at 18,800 days).

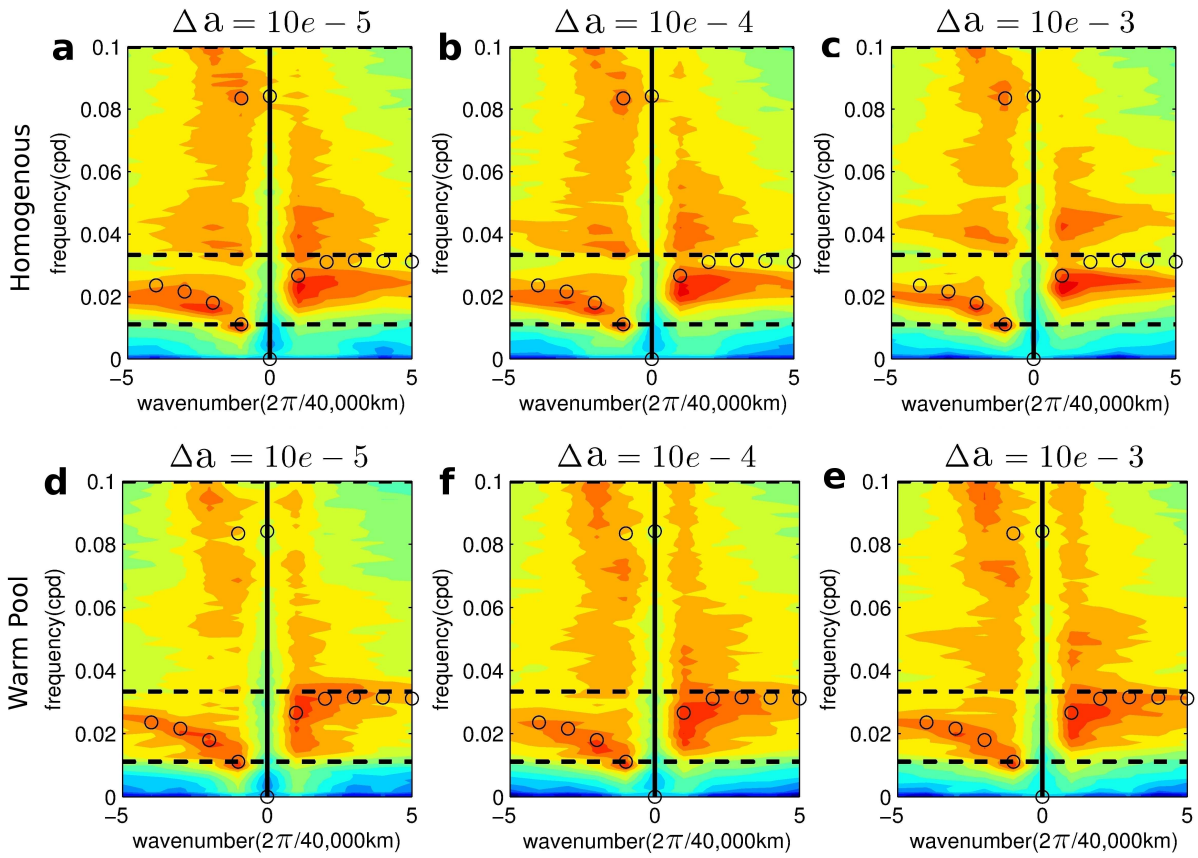

Figure 10: Sensitivity to Δa: Zonal wavenumber-frequency power spectra of u, for (a) $\Delta a = 10^{-5}$, (b) $\Delta a = 10^{-4}$, and (c) $\Delta a = 10^{-3}$, as a function of zonal wavenumber (in $2\pi/40000km$) and frequency (in cpd), for simulations with a homogeneous background state. (d)(e)(f) repeats the graphs for simulations with background warm pool state. Figure setup is identical to the one of figure 2 and figure 7.